

See discussions, stats, and author profiles for this publication at: <https://www.researchgate.net/publication/236066483>

# Electroluminescence In Single Layer MoS<sub>2</sub>.

ARTICLE in NANO LETTERS · MARCH 2013

Impact Factor: 13.59 · DOI: 10.1021/nl400516a · Source: PubMed

---

CITATIONS

183

---

READS

88

7 AUTHORS, INCLUDING:



Michael Engel

IBM

32 PUBLICATIONS 898 CITATIONS

SEE PROFILE



Antonio Lombardo

University of Cambridge

49 PUBLICATIONS 2,956 CITATIONS

SEE PROFILE



Ralph Krupke

Karlsruhe Institute of Technology

95 PUBLICATIONS 3,939 CITATIONS

SEE PROFILE



Phaedon Avouris

IBM, T. J. Watson Research Center

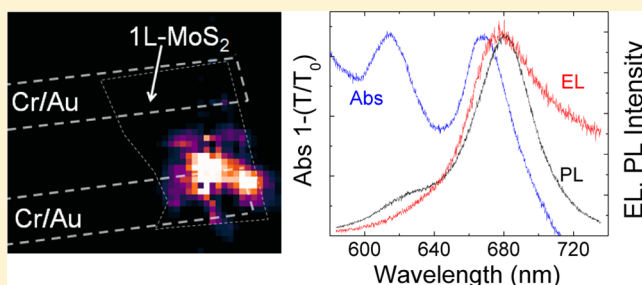
520 PUBLICATIONS 45,921 CITATIONS

SEE PROFILE

Electroluminescence in Single Layer MoS<sub>2</sub>R. S. Sundaram,<sup>†</sup> M. Engel,<sup>‡</sup> A. Lombardo,<sup>†</sup> R. Krupke,<sup>‡,§</sup> A. C. Ferrari,<sup>†</sup> Ph. Avouris,<sup>\*,||</sup> and M. Steiner<sup>\*,||</sup><sup>†</sup>Cambridge Graphene Centre, University of Cambridge, 9 JJ Thomson Avenue, Cambridge CB3 0FA, United Kingdom<sup>‡</sup>Institute of Nanotechnology, Karlsruhe Institute of Technology, 76021 Karlsruhe, Germany<sup>§</sup>Institut für Materialwissenschaft, Technische Universität Darmstadt, 64287 Darmstadt, Germany<sup>||</sup>IBM Thomas J. Watson Research Center, Yorktown Heights, New York 10598, United States

**ABSTRACT:** We detect electroluminescence in single layer molybdenum disulfide (MoS<sub>2</sub>) field-effect transistors built on transparent glass substrates. By comparing the absorption, photoluminescence, and electroluminescence of the same MoS<sub>2</sub> layer, we find that they all involve the same excited state at 1.8 eV. The electroluminescence has pronounced threshold behavior and is localized at the contacts. The results show that single layer MoS<sub>2</sub>, a direct band gap semiconductor, could be promising for novel optoelectronic devices, such as two-dimensional light detectors and emitters.

**KEYWORDS:** MoS<sub>2</sub>, photoluminescence, electroluminescence, photocurrent microscopy, nano-optics



Molybdenum disulfide (MoS<sub>2</sub>), a layered quasi-two-dimensional (2D) chalcogenide material,<sup>1</sup> is subject of intense research because of its electronic<sup>2</sup> and optical properties,<sup>3</sup> such as strong photoluminescence (PL),<sup>3,4</sup> controllable valley and spin polarization,<sup>5,6</sup> and a large on–off ratio in field effect transistors (FETs).<sup>2</sup> A single layer of MoS<sub>2</sub> (1L-MoS<sub>2</sub>) consists of two planes of hexagonally arranged S atoms linked to a hexagonal plane of Mo atoms via covalent bonds.<sup>3,7–10</sup> In the bulk, individual MoS<sub>2</sub> layers are held together by weak van der Waals forces.<sup>7–10</sup> This property has been exploited in lubrication technology<sup>11</sup> and, more recently, has led to the isolation of single MoS<sub>2</sub> layers.<sup>2–4,12</sup> While bulk MoS<sub>2</sub> is a semiconductor with an indirect band gap of 1.3 eV,<sup>13</sup> 1L-MoS<sub>2</sub> has a direct band gap of 1.8 eV.<sup>3,4</sup> The absence of interlayer coupling of electronic states at the  $\Gamma$  point of the Brillouin zone in 1L-MoS<sub>2</sub><sup>4,14</sup> results in strong absorption and PL bands at  $\sim$ 1.8 eV (680 nm).<sup>3,4</sup> 1L-MoS<sub>2</sub> FETs have good transport characteristics with mobilities<sup>2</sup>  $>60$  cm<sup>2</sup> V<sup>−1</sup> s<sup>−1</sup> and on–off current ratios up to 10<sup>8</sup>.<sup>2</sup> Samples thicker than 10 nm were studied in refs 14–16 and show both unipolar<sup>2</sup> and ambipolar<sup>14</sup> transport with mobilities<sup>15</sup>  $>480$  cm<sup>2</sup> V<sup>−1</sup> s<sup>−1</sup> and on–off ratios up to 10<sup>9</sup>.<sup>16</sup> The combination of these electrical and optical properties makes 1L-MoS<sub>2</sub> a promising candidate for novel optoelectronic devices, such as 2D photodetectors,<sup>17–19</sup> and light-emitting devices operating in the visible range.

Here, we report electrically excited luminescence in 1L-MoS<sub>2</sub> devices and study the underlying emission mechanism. We find that the electroluminescence occurs via hot carrier processes and is localized in the region of the contacts. The observed photoluminescence and electroluminescence arise from the same excited state at 1.8 eV.

1L-MoS<sub>2</sub> flakes are produced by micromechanical cleavage of bulk MoS<sub>2</sub> crystals (Structure Probe Inc.-SPI, natural molybdenite) on 100 nm SiO<sub>2</sub>. As for the case of graphene,<sup>20</sup> interference allows visibility and counting the number of layers, Figure 1a. Due to the different dielectric properties, an optimum thickness of 100 nm SiO<sub>2</sub> is well suited for MoS<sub>2</sub>.<sup>21</sup> The presence of monolayers is then confirmed by performing PL measurements. The PL spectrum of 1L-MoS<sub>2</sub> exhibits two bands at 2 eV and 1.8 eV (Figure 1b) associated with excitonic transitions at the K point of the Brillouin zone.<sup>4</sup> The energy difference of 0.2 eV has been attributed to the degeneracy breaking of the valence band due to spin–orbit coupling.<sup>4,7,8,22</sup> As compared to bulk MoS<sub>2</sub>, Figure 1b, 1L-MoS<sub>2</sub> does not have a peak at 1.4 eV,<sup>3,4</sup> associated with the indirect band gap.<sup>12</sup> In addition, 1L-MoS<sub>2</sub> exhibits a stronger PL compared to bulk MoS<sub>2</sub>,<sup>3,4</sup> due to the direct band gap. Another evidence for 1L-MoS<sub>2</sub> comes from the analysis of the Raman spectra, Figure 1d. The peak at  $\sim$ 385 cm<sup>−1</sup> corresponds to the in plane (E<sub>1g</sub>) mode,<sup>23,24</sup> while that at  $\sim$ 404 cm<sup>−1</sup> is attributed to the out of plane (A<sub>1g</sub>) mode.<sup>23,24</sup> The E<sub>1g</sub> mode softens, and A<sub>1g</sub> mode stiffens with increasing layer thickness,<sup>23,24</sup> similar to what happens for other layered materials, where the bond distance changes with number of layers.<sup>25</sup> The frequency difference between these two modes of 19 cm<sup>−1</sup> observed in the Raman spectrum in Figure 1d can be used as an indicator of 1L-MoS<sub>2</sub>.<sup>23</sup> This difference can also change as a function of doping.<sup>26</sup>

1L-MoS<sub>2</sub> flakes are then transferred onto glass substrates by using a poly(methyl methacrylate) (PMMA)-based technique, similar to that previously used to transfer graphene onto optical

Received: November 15, 2012

Published: March 20, 2013

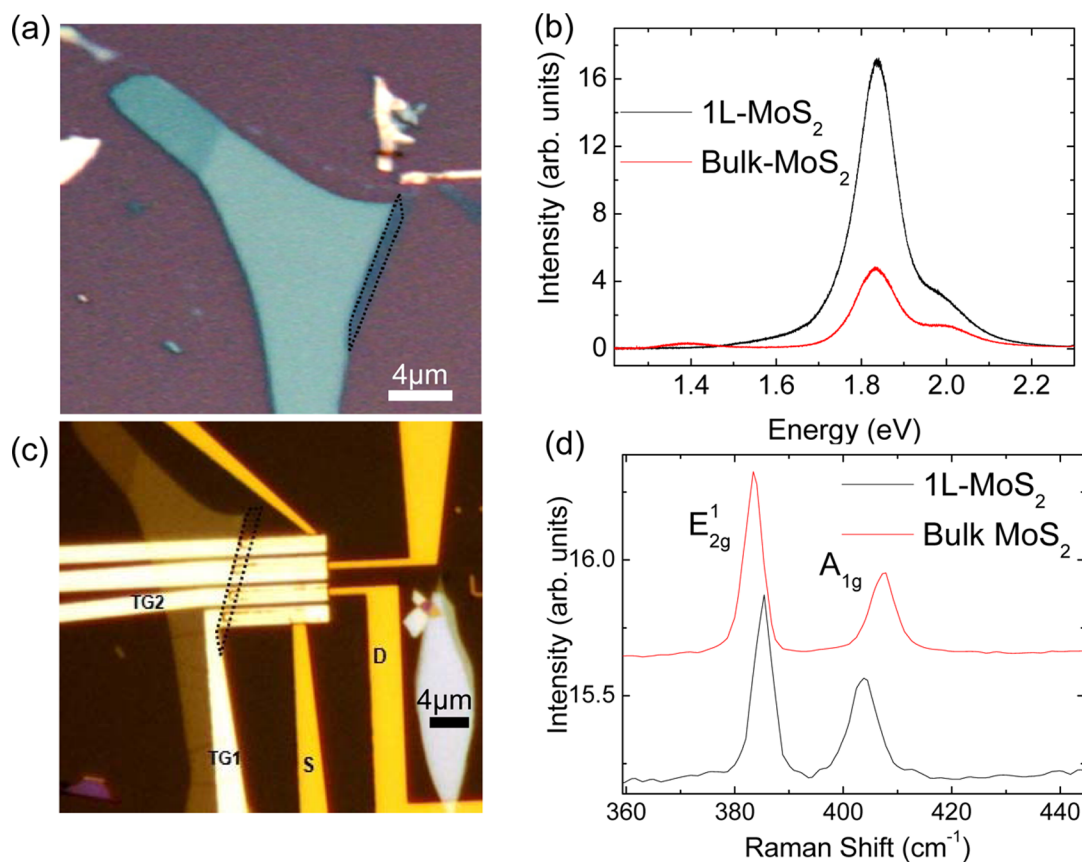


**Figure 1.** (a) Optical white light microscope image of a MoS<sub>2</sub> flake. The monolayer region is highlighted by dashed lines. (b) PL spectrum measured on (red) bulk MoS<sub>2</sub> and (black) 1L-MoS<sub>2</sub> for 514.5 nm excitation. The PL is stronger for 1L-MoS<sub>2</sub>. (c) Optical image of the MoS<sub>2</sub> devices with source (S), drain (D), and top gate electrodes (TG1, TG2). The 1L-MoS<sub>2</sub> position is highlighted by the black dashed line. (d) Raman spectra at 514.5 nm excitation in (top) bulk MoS<sub>2</sub> and (bottom) 1L-MoS<sub>2</sub>. The difference in peak positions identifies the monolayer.<sup>24</sup>

fiber cores.<sup>27,28</sup> This process involves spin coating two layers of 495K PMMA and one layer of 950K PMMA on the substrate where flakes are deposited. The samples are subsequently immersed in deionized (DI) water at 90 °C for 1 h, resulting in the detachment of the polymer film, due to the intercalation of water at the polymer–SiO<sub>2</sub> interface. MoS<sub>2</sub> flakes stick to the PMMA and can thus be removed from the original substrate and transferred onto glass substrates.<sup>27,28</sup> To manufacture a device with split top gates, we use standard e-beam lithography to define source and drain contacts, followed by thermal evaporation of Au (50 nm) with a Cr adhesion layer (2 nm). This low Cr thickness is sufficient for the adhesion of 50 nm Au, typically used as source-drain contacts in MoS<sub>2</sub> transistors.<sup>2</sup> The gate dielectric is then made via atomic layer deposition (ALD) of Al<sub>2</sub>O<sub>3</sub> (30 nm). This thickness was previously used for electrostatic p–n junctions in nanotubes, and offers a compromise between film uniformity and gate capacitance.<sup>26</sup> Top gate electrodes are then made by evaporating 50 nm Au with a 2 nm Cr adhesion layer (Figure 1c).

Our experimental setup combines an electrical transport measurement system with an inverted optical microscope equipped with a multiaxis stage for raster scanning the devices with respect to a tightly focused laser beam (diameter ~ 250 nm,  $\lambda = 514.5$  nm, immersion objective, NA = 1.25).<sup>29,30</sup> Electrical measurements are performed by converting the short-circuit photocurrent between the source and drain (ground) electrodes into a voltage signal by using a current preamplifier and a source meter synchronized with a controlling computer

and an optical scanning system, using the setup sketched in Figure 2a. Optical spectroscopy is done via a liquid-nitrogen cooled, back-illuminated, deep-depleted charge coupled device (CCD) and a 300 grooves/mm grating, as for refs 29–31.

Figure 2b shows the transfer characteristics acquired by sweeping both top gates simultaneously at a drain-source voltage  $V_D = 200$  mV. The device has a 2 M $\Omega$  on-state resistance and on–off ratio 10<sup>3</sup>. The inset Figure 2b shows the behavior of the output current for different settings of split gate voltages, having either equal or opposite polarity. While the efficacy of the split gate in modulating the current is limited, we observe some nonlinearity in the measured  $I$ – $V$  curves, with a reproducible dependence on varying split gate voltages.

Figure 3a plots an elastic scattering image of the device, taken by raster scanning a 20  $\times$  20  $\mu\text{m}^2$  area with a 50 nm step size and acquired in confocal mode with laser illumination at 514.5 nm, through the immersion objective, and with a single photon counting module in the detection path. PL images are recorded with laser power density  $P_{\text{Laser}} < 100$  kW/cm<sup>2</sup> through a band-pass filter centered at 700 nm. Figure 3b plots the PL map of the same device imaged in Figure 3a. The PL intensity is higher at the 1L-MoS<sub>2</sub> position, as expected.<sup>3,4</sup> The PL appears further enhanced underneath the metal gates, a result of the higher collection efficiency due to reflection. In contrast, the PL is quenched at the MoS<sub>2</sub>–Cr/Au interface, with no significant PL at the source and drain contacts.

To map the electrostatic potential profiles within our device, we employ raster scanning photocurrent microscopy. Exfoliated

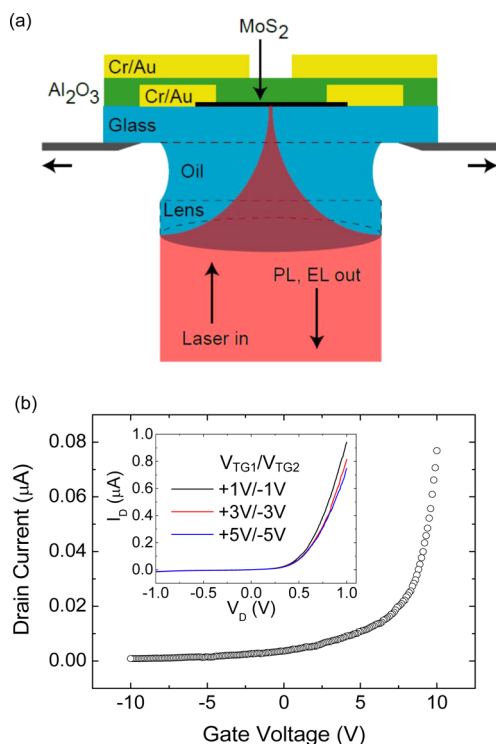


**Figure 2.** (a) Schematic of a top-gated MoS<sub>2</sub> FET and the optical setup. (b) Electrical transfer characteristics of a 1L-MoS<sub>2</sub> FET at bias voltage  $V_D = 200$  mV. (Inset) Electrical output characteristics of a 1L-MoS<sub>2</sub> FET. The gate voltage pairs ( $V_{TG1}/V_{TG2}$ ) applied during the  $V_D$  sweep are also indicated.

1L-MoS<sub>2</sub> behaves as an n-doped semiconductor, with a Fermi level at 4.7 eV ( $\Phi_{\text{MoS}_2}$ ).<sup>2,17,32</sup> The intrinsic doping has been assigned to halogen (Cl or Br) impurities in natural MoS<sub>2</sub> crystals.<sup>17</sup> If MoS<sub>2</sub> is brought in contact with Cr/Au, having work functions  $\Phi_{\text{Cr/Au}} = 4.8$  eV<sup>33</sup> to 5.1 eV,<sup>17</sup> a Schottky barrier ( $\Phi_{\text{SB}}$ ) is formed with a height of 100 to 400 meV [ $\Phi_{\text{SB}} = \Phi_{\text{Cr/Au}} - \Phi_{\text{MoS}_2}$ ], and we expect a strong photocurrent response at the contacts, similar to other 1D and 2D nanostructures, such as carbon nanotubes,<sup>34</sup> silicon nanowires,<sup>35</sup> and graphene.<sup>36</sup> Figure 4a plots the accumulated photocurrent cross sections recorded by raster scanning the device with respect to the focused laser beam. After image acquisition, the photocurrent is measured along the direction perpendicular to the device channel and overlaid with the position of drain–source contacts and top gates for three representative top gate voltage settings. The photocurrent response at the contact edges is mainly due to the Schottky barriers at the MoS<sub>2</sub>–Cr/Au interface. Ideally, we expect that p- and n-type regions in the MoS<sub>2</sub> channel could be created by using electrostatic doping through the application of appropriate split gate voltages, as previously shown in nanotubes<sup>29,37,38</sup> and graphene.<sup>39</sup> However, due to the large band gap (1.8 eV) in 1L-MoS<sub>2</sub>, even for the highest electrostatic potential difference (+10 V/–10 V) we observe only a weak effect on the measured photocurrent amplitude (Figure 4a), consistent with low doping levels ( $<0.2 \times 10^{13}$  cm<sup>–2</sup>) at these top gate voltages. While we find that the Schottky barrier for electron injection can be modulated through the application of the respective split gate voltages, we do not observe significant hole currents in both photocurrent and electrical transport measurements. As a result, our gating configuration is inefficient for creating a p–n junction within

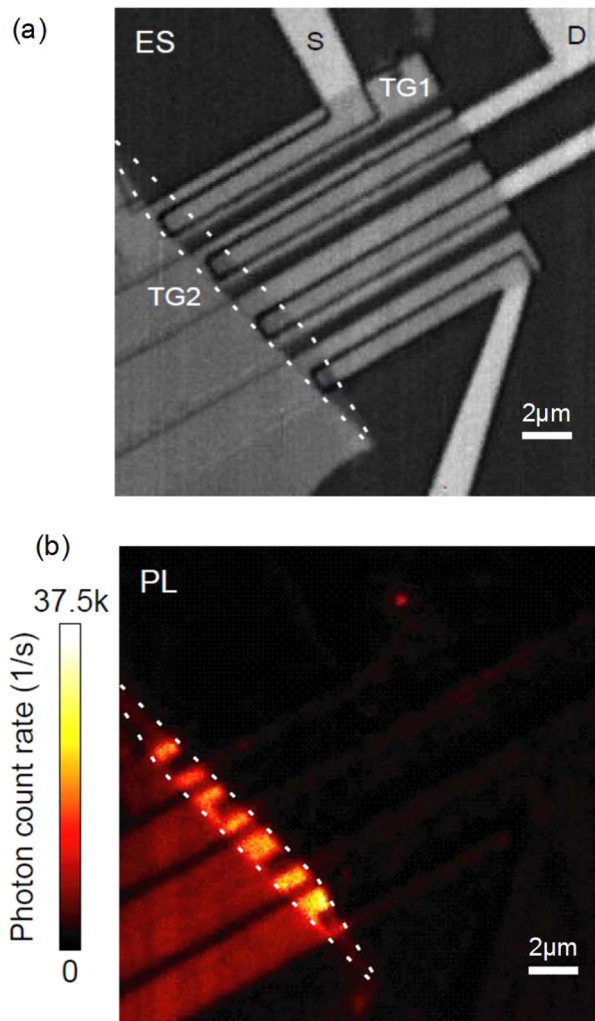


**Figure 3.** (a) Elastic scattering (ES) image taken from the underside of the MoS<sub>2</sub> device array reveals the position of source (S) and drain (D) contacts and the top gate electrodes (TG1, TG2). (b) The PL image of the same area reveals the 1L-MoS<sub>2</sub> position within the device array highlighted in (a) by white dashed lines.

the device, as evidenced in the electrostatic potential profiles in Figure 4b, generated by numerically integrating the accumulated photocurrent amplitudes in Figure 4a. This has important implications for the electrical detection and generation of light emission within the present device configuration. The conversion efficiencies of photons to carriers (or carriers to photons) cannot be controlled by the gates in the present case and are largely determined by the internal device electrostatics.

Since electrons and holes cannot be injected independently into the MoS<sub>2</sub> channel, we exploit hot carrier processes for measuring the electroluminescence (EL) spectrum of 1L-MoS<sub>2</sub>. At high bias, electrons injected into the conduction band should experience a strong band bending at the MoS<sub>2</sub>–metal contact, with generation of excitons via impact excitation, a process extensively studied in semiconducting nanotubes.<sup>40</sup> Also, a bipolar EL mechanism under unipolar, high bias conditions, such as that reported in ref 44, could occur. In this case, electrons (majority carriers) would be backscattered and accumulated near a drain contact and promote hole leakage (minority carriers) from the drain electrode, resulting in radiative recombination. Additionally, we observe an exponen-



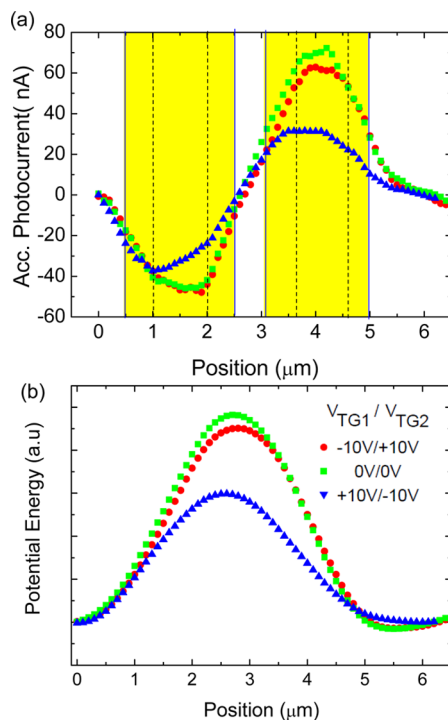


**Figure 4.** Normalized photocurrent measured from the underside of a MoS<sub>2</sub> device for three representative split gate voltage pairs ( $V_{TG1}/V_{TG2}$ ): (-10 V/+10 V) red circles, (0 V/0 V) green squares, (+10 V/-10 V) blue triangles. The curves represent the total photocurrent accumulated perpendicular to the channel direction, based on the measured photocurrent images and a linear background correction. The position of source and drain contacts is indicated by dashed black lines, the position of the top gates by the golden areas. (b) Internal electrostatic potential cross sections of the MoS<sub>2</sub> device for three split gate voltage pairs. The curves are obtained by numerically integrating the experimental photocurrent data in (a).

tial background below the EL peak in Figure 5b. This implies a significant heating of 1L-MoS<sub>2</sub> at high bias, similar to graphene,<sup>31,41–43</sup> which could result in a thermal population of the emitting state.

In our experiment, we determine the optimum EL bias by tuning the source drain voltage while mapping the EL emission by means of a single photon counting detector. Figure 5a shows the EL spectrum of 1L-MoS<sub>2</sub>. The spectral distribution has a full-width-at-half-maximum (FWHM)  $\sim 40$  nm, and a peak position  $\sim 685$  nm. For comparison, we plot a high-bias EL spectrum along with PL and absorption spectra in Figure 5b. The two principal absorption features at 610 and 670 nm are associated with the A and B excitons of MoS<sub>2</sub>.<sup>3–5</sup> Their positions correspond well with the observed PL peaks at 620 and 680 nm. A Stokes shift of  $\sim 10$  nm separates the spectral positions of the absorption and PL peaks. We assign this to surface interaction of 1L-MoS<sub>2</sub> within the inhomogeneous dielectric environment (substrate SiO<sub>2</sub>, gate dielectric Al<sub>2</sub>O<sub>3</sub>), which in turn influences the exciton binding energy due to screening of the electron–hole Coulomb interaction.<sup>45</sup> Importantly, the peak position in the EL spectrum matches the PL peak at  $\sim 680$  nm, evidencing that EL and PL emission involve the same excited state, i.e., the B exciton. However, the PL feature at 620 nm cannot be observed in the EL spectrum, highlighting that the excitation mechanisms in PL and EL are different. The electrical power density ( $P_{El} = V_d I_d / L_c W_c$ ) provided through impact excitation is not high enough to

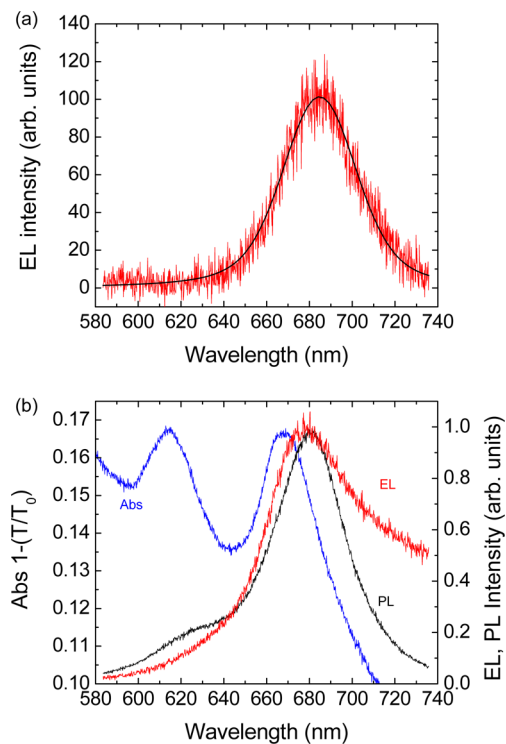


**Figure 5.** (a) EL spectrum of a 1L-MoS<sub>2</sub> device measured at  $V_D = 5$  V and  $I_D = 100$   $\mu$ A, with a Voigt fit. (b) Absorption (Abs), EL, and PL spectra on the same 1L-MoS<sub>2</sub>. The EL spectrum is measured at  $V_D = 8$  V and  $I_D = 164$   $\mu$ A.

efficiently populate the higher energy excitonic state, thus precluding a significant spectroscopic signature at 620 nm in the measured EL spectra (i.e.,  $\sim 50\%$  of the intensity of the 680 nm peak like in the PL spectra). Moreover, the weaker B excitonic state at 620 nm was previously assigned to charged excitons formed when photogenerated excitons bind to free electrons.<sup>5</sup> The low EL efficiency (as compared to PL) makes it less likely for such a process to occur. While high electrical bias causes spectral broadening and increased thermal background in the EL spectrum (see Figure 5b), we do not observe significant spectral shifts.

To investigate the threshold behavior and the efficiency of EL generation we plot in Figure 6a the integrated light intensity as function of electrical power density injected into the MoS<sub>2</sub> channel of a different device (channel length  $L_c = 1.5$   $\mu$ m, channel width  $W_c = 2.3$   $\mu$ m,  $I_d$ - $V_d$  curve under operating conditions shown in inset of Figure 6a). We observe significant light emission only above a threshold power density of 15 kW/cm<sup>2</sup>. The reason is that the electrons need to acquire sufficient kinetic or thermal energy for the generation of excitons. The EL threshold bias hence depends on the exciton binding energy and the thermal properties of the channel material, as well as the specifics of the semiconductor–metal contacts of the actual device. The exciton-to-phonon conversion efficiency is calculated by dividing the integrated photon count rate (Figure 6a) by the quantum efficiency of the detector, the fraction of light detected within the solid angle (based on the NA of the objective), and the losses of light when it passes through the objective and mirrors along the optical path. This gives us the total photon flux originating from the sample. When putting this in relation to the current, i.e., carriers per unit time, we arrive at a conservative estimate of the conversion efficiency of

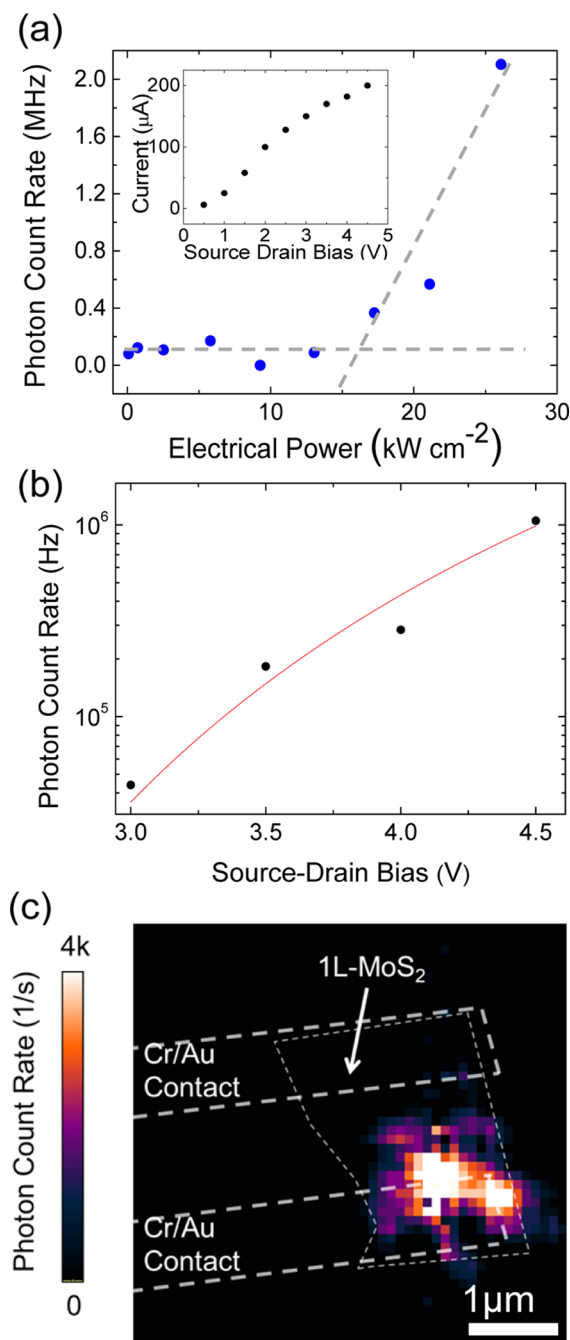


**Figure 6.** (a) EL count rate as function of injected electrical power density for a different 1L-MoS<sub>2</sub> device with respect to that shown in Figure 1. Each data point represents the sum of all photon counts recorded within an image of the entire device area at a given electrical power density. The dark count rate is  $\sim 0.09$  MHz for the entire measurement. The dashed lines are a guide to the eyes. The inset shows the current–voltage characteristics of the device under operating conditions. (b) Photon count rate plotted as a function of applied bias. The red solid line is a fit to the impact ionization model similar to ref 46. (c) False color image showing EL emission in the vicinity of a contact edge. The positions of Cr/Au contacts are highlighted by thick dashed lines (white), and the MoS<sub>2</sub> layer is indicated by thin dashed lines (gray). The device is biased at  $V_D = 4$  V and  $I_D = 180$   $\mu$ A.

$\sim 10^{-5}$ . For a comparison, this is at least an order of magnitude lower than thus far reported for individual semiconducting single walled nanotubes.<sup>38</sup> The conversion efficiency could be

enhanced significantly by creating a p–n structure that enables threshold-less carrier recombination. Furthermore, we estimate the length of the EL active zone following the procedure of ref 46 by plotting EL intensity as a function of source–drain bias (Figure 6b). We estimate the threshold electric field using  $F_{th} \sim 1.5E_{gap}/(e \times \lambda_{opticalphonon})$  and assuming  $\lambda_{opticalphonon} = 14$  nm at 300 K<sup>47</sup> with  $E_{gap} = 1.9$  eV. This gives  $F_{th} \sim 2$  MV cm<sup>-1</sup>, similar to that reported for individual CdSe nanowires with  $E_{gap} = 1.7$  eV.<sup>46</sup> Using the fit function  $f = k \exp(-E_{threshold}/E_{local})$ , where  $E_{local} = V_{Threshold}/w_{activezone}$ , our best estimate for the EL active zone is  $(150 \pm 5)$  nm, i.e., below our experimental resolution.

Since hot carrier effects rely on strong band deformation,<sup>48</sup> the efficiency of exciton generation through impact excitation and thermal population should be maximized at the positions where the carrier injection occurs, i.e. at the source and drain electrodes. We hence expect EL not homogeneously radiated from the 1L-MoS<sub>2</sub>, but spatially localized near the contacts. To map the EL spatial distribution within the 1L-MoS<sub>2</sub> FET, we raster scan EL images of the biased device with a single photon counting module through a band-pass filter centered at 700 nm. From an elastic laser scattering image of the device acquired with the same detector, we are able to locate the position of source and drain contacts with high precision. By overlaying the contact positions in the EL image shown in Figure 6c, we find that the EL emission is indeed localized at one of the metal contacts.

To exploit 1L-MoS<sub>2</sub> in practical optoelectronic devices, the efficiency of light detection and emission needs to be significantly enhanced. Novel device designs are needed to improve yield and control charge carrier injection and extraction, such as the use of highly efficient gates to create electrostatic p–n junctions. An alternative could be the use of strong doping via polymer electrolytes<sup>49</sup> or intercalation.<sup>50</sup>

In conclusion, single layer MoS<sub>2</sub> transistors can detect and emit visible light. Both photoluminescence and electroluminescence arise from the same excited state at 1.8 eV. Better electrostatic gating techniques are needed to improve control and efficiency of light emission and detection in optoelectronic devices made of MoS<sub>2</sub>.

## AUTHOR INFORMATION

### Corresponding Author

\*E-mail: avouris@us.ibm.com, msteine@us.ibm.com.

### Notes

The authors declare no competing financial interest.

## ACKNOWLEDGMENTS

We acknowledge funding from EU grants NANOPOTS, GENIUS, EPSRC grants EP/G042357/1, EP/K01711X/1, EP/K017144/1, a Royal Society Wolfson Research Merit Award, and St. Edmund's College, Cambridge.

## REFERENCES

- (1) Frindt, R. F. *J. Appl. Phys.* **1966**, 37 (4), 1928–1929.
- (2) Radisavljevic, B.; Radenovic, A.; Brivio, J.; Giacometti, V.; Kis, A. *Nat. Nanotechnol.* **2011**, 6 (3), 147–150.
- (3) Mak, K. F.; Lee, C.; Hone, J.; Shan, J.; Heinz, T. F. *Phys. Rev. Lett.* **2010**, 105 (13), 136805.
- (4) Splendiani, A.; Sun, L.; Zhang, Y.; Li, T.; Kim, J.; Chim, C.-Y.; Galli, G.; Wang, F. *Nano Lett.* **2010**, 10 (4), 1271–1275.
- (5) Mak, K. F.; He, K.; Shan, J.; Heinz, T. F. *Nat. Nanotechnol.* **2012**, 7 (8), 494–498.

- (6) Zeng, H.; Dai, J.; Yao, W.; Xiao, D.; Cui, X. *Nat. Nanotechnol.* **2012**, *7* (8), 490–493.
- (7) Böker, T.; Severin, R.; Müller, A.; Janowitz, C.; Manzke, R.; Voß, D.; Krüger, P.; Mazur, A.; Pollmann, J. *Phys. Rev. B* **2001**, *64* (23), 235305.
- (8) Coehoorn, R.; Haas, C.; Dijkstra, J.; Flipse, C. J. F.; de Groot, R. A.; Wold, A. *Phys. Rev. B* **1987**, *35* (12), 6195–6202.
- (9) Coehoorn, R.; Haas, C.; de Groot, R. A. *Phys. Rev. B* **1987**, *35* (12), 6203–6206.
- (10) Mattheiss, L. F. *Phys. Rev. B* **1973**, *8* (8), 3719–3740.
- (11) Kim, Y.; Huang, J.-L.; Lieber, C. M. *Appl. Phys. Lett.* **1991**, *59* (26), 3404–3406.
- (12) Novoselov, K. S. *Science* **2004**, *306*, 666–669.
- (13) Kam, K. K.; Parkinson, B. A. *J. Phys. Chem.* **1982**, *86* (4), 463–467.
- (14) Li, T.; Galli, G. *J. Phys. Chem. C* **2007**, *111* (44), 16192–16196.
- (15) Bao, W.; Cai, X.; Kim, D.; Sridhara, K.; Fuhrer, M. S. *Appl. Phys. Lett.* **2013**, *102*, 042104.
- (16) Liu, H.; Neal, A. T.; Ye, P. D. *ACS Nano* **2012**, *6* (10), 8563–8569.
- (17) Yin, Z.; Li, H.; Li, H.; Jiang, L.; Shi, Y.; Sun, Y.; Lu, G.; Zhang, Q.; Chen, X.; Zhang, H. *ACS Nano* **2012**, *6* (1), 74–80.
- (18) Alkis, S.; Özta, T.; Aygün, L. E.; Bozkurt, F.; Okyay, A. K.; Ortaç, B. *Opt. Express* **2012**, *20* (19), 21815–21820.
- (19) Lee, H. S.; Min, S.-W.; Chang, Y.-G.; Park, M. K.; Nam, T.; Kim, H.; Kim, J. H.; Ryu, S.; Im, S. *Nano Lett.* **2012**, *12* (7), 3695–3700.
- (20) Casiraghi, C.; Hartschuh, A.; Lidorikis, E.; Qian, H.; Harutyunyan, H.; Gokus, T.; Novoselov, K. S.; Ferrari, A. C. *Nano Lett.* **2007**, *7* (9), 2711–2717.
- (21) Benameur, M. M.; Radisavljevic, B.; Héron, J. S.; Sahoo, S.; Berger, H.; Kis, A. *Nanotechnol.* **2011**, *22* (12), 125706.
- (22) Korn, T.; Heydrich, S.; Hirmer, M.; Schmutzler, J.; Schuller, C. *Appl. Phys. Lett.* **2011**, *99* (10), 102109–3.
- (23) Lee, C.; Yan, H.; Brus, L. E.; Heinz, T. F.; Hone, J.; Ryu, S. *ACS Nano* **2010**, *4* (5), 2695–2700.
- (24) Zhang, X.; Han, W. P.; Wu, J. B.; Milana, S.; Lu, Y.; Li, Q. Q.; Ferrari, A. C.; Tan, P. H. *Phys. Rev. B* **2013**, *87*, 115413.
- (25) Arenal, R.; Ferrari, A. C.; Reich, S.; Wirtz, L.; Mevellec, J. Y.; Lefrant, S.; Rubio, A.; Loiseau, A. *Nano Lett.* **2006**, *6* (8), 1812–1816.
- (26) Chakraborty, B.; Bera, A.; Muthu, D. V. S.; Bhowmick, S.; Waghmare, U. V.; Sood, A. K. *Phys. Rev. B* **2012**, *85*, 161403.
- (27) Bonaccorso, F.; Sun, Z.; Hasan, T.; Ferrari, A. C. *Nat. Photonics* **2010**, *4* (9), 611–622.
- (28) Bonaccorso, F.; Lombardo, A.; Hasan, T.; Sun, Z.; Colombo, L.; Ferrari, A. C. *Mater. Today* **2012**, *15*, 564.
- (29) Engel, M.; Steiner, M.; Sundaram, R. S.; Krupke, R.; Green, A. A.; Hersam, M. C.; Avouris, P. *ACS Nano* **2012**, *6* (8), 7303–7310.
- (30) Sundaram, R. S.; Steiner, M.; Chiu, H.-Y.; Engel, M.; Bol, A. A.; Krupke, R.; Burghard, M.; Kern, K.; Avouris, P. *Nano Lett.* **2011**, *11* (9), 3833–3837.
- (31) Engel, M.; Steiner, M.; Lombardo, A.; Ferrari, A. C.; Löhneysen, H. v.; Avouris, P.; Krupke, R. *Nat. Commun.* **2012**, *3*, 906.
- (32) Novoselov, K. S.; Jiang, D.; Schedin, F.; Booth, T. J.; Khotkevich, V. V.; Morozov, S. V.; Geim, A. K. *Proc. Natl. Acad. Sci. U.S.A.* **2005**, *102* (30), 10451–10453.
- (33) Riviere, J. C. *Solid State Surface Science*; Decker: New York, 1969; Vol. 1.
- (34) Lee, E. J. H.; Balasubramanian, K.; Dorfmueller, J.; Vogelgesang, R.; Fu, N.; Mews, A.; Burghard, M.; Kern, K. *Small* **2007**, *3* (12), 2038–2042.
- (35) Allen, J. E.; Hemesath, E. R.; Lauhon, L. J. *Nano Lett.* **2009**, *9* (5), 1903–1908.
- (36) Burghard, M.; Mews, A. *ACS Nano* **2012**, *6* (7), 5752–5756.
- (37) Kinoshita, M.; Steiner, M.; Engel, M.; Small, J. P.; Green, A. A.; Hersam, M. C.; Krupke, R.; Mendez, E. E.; Avouris, P. *Opt. Express* **2010**, *18* (25), 25738–25745.
- (38) Mueller, T.; Kinoshita, M.; Steiner, M.; Perebeinos, V.; Bol, A. A.; Farmer, D. B.; Avouris, P. *Nat. Nanotechnol.* **2010**, *5* (1), 27–31.
- (39) Gabor, N. M.; Song, J. C. W.; Ma, Q.; Nair, N. L.; Taychatanapat, T.; Watanabe, K.; Taniguchi, T.; Levitov, L. S.; Jarillo-Herrero, P. *Science* **2011**, *334* (6056), 648–652.
- (40) Avouris, P.; Freitag, M.; Perebeinos, V. *Nat. Photonics* **2008**, *2* (6), 341–350.
- (41) Freitag, M.; Steiner, M.; Martin, Y.; Perebeinos, V.; Chen, Z.; Tsang, J. C.; Avouris, P. *Nano Lett.* **2009**, *9* (5), 1883–1888.
- (42) Berciaud, S.; Han, M. Y.; Mak, K. F.; Brus, L. E.; Kim, P.; Heinz, T. F. *Phys. Rev. Lett.* **2010**, *104* (22), 227401.
- (43) Freitag, M.; Chiu, H.-Y.; Steiner, M.; Perebeinos, V.; Avouris, P. *Nat. Nanotechnol.* **2010**, *5*, 497.
- (44) Adam, E.; Aguirre, C. M.; Marty, L.; St-Antoine, B. C.; Meunier, F.; Desjardins, P.; Ménard, D.; Martel, R. *Nano Lett.* **2008**, *8* (8), 2351–2355.
- (45) Plechinger, G.; Schrettenbrunner, F. X.; Eroms, J.; Weiss, D.; Schüller, C.; Korn, T. *Phys. Status Solidi (RRL)* **2012**, *6* (3), 126–128.
- (46) Doh, Y.-J.; Maher, K. N.; Ouyang, L.; Yu, C. L.; Park, H.; Park, J. *Nano Lett.* **2008**, *8* (12), 4552–4556.
- (47) Kaasbjerg, K.; Thygesen, K. S.; Jacobsen, K. W. *Phys. Rev. B* **2012**, *85*, 115317.
- (48) Freitag, M.; Perebeinos, V.; Chen, J.; Stein, A.; Tsang, J. C.; Misewich, J. A.; Martel, R.; Avouris, P. *Nano Lett.* **2004**, *4* (6), 1063–1066.
- (49) Das, A.; Pisana, S.; Chakraborty, B.; Piscanec, S.; Saha, S. K.; Waghmare, U. V.; Novoselov, K. S.; Krishnamurthy, H. R.; Geim, A. K.; Ferrari, A. C.; Sood, A. K. *Nat. Nanotechnol.* **2008**, *3* (4), 210–215.
- (50) Zhao, W.; Tan, P. H.; Liu, J.; Ferrari, A. C. *J. Am. Chem. Soc.* **2011**, *133* (15), 5941–5946.